electronics

Article

Design and Performance Analysis of a Permanent Magnet Assisted Line-Start Synchronous Reluctance Motor with Nonoverlapping Winding

Syed Toqeer Haider [1,*], Faisal Khan [1,*], Abdoalateef Alzhrani [2], Dae Yong Um [3,*] and Wasiullah Khan [1]

[1] Department of Electrical Engineering, COMSATS University Islamabad, Abbottabad Campus, Abbottabad 22060, Pakistan; wasiullahkhan2001@gmail.com
[2] Department of Electrical Engineering, Jubail Industrial College, Jubail 31961, Saudi Arabia; abdoalateef@gmail.com
[3] Department of Electrical Engineering, Gyeongsang National University, Jinju-si 52828, Republic of Korea
* Correspondence: stoqeerhaider@gmail.com (S.T.H.); faisalkhan@cuiatd.edu.pk (F.K.); daeyongum@gnu.ac.kr (D.Y.U.)

Abstract

This study presents a systematic topological progression and multi-objective optimization of a Permanent Magnet-assisted Non-overlapping Winding Line-Start Synchronous Reluctance Motor (PMaNWLS-SynRM) for industrial applications. To explicitly highlight the core contribution, the research establishes a rigorous comparative framework evaluating the transition from a conventional 4-pole/36-slot distributed winding (DW) to a 2 × 12-slot non-overlapping winding (NW) architecture. Baseline results demonstrate that the NW configuration shortens end-turns, successfully reducing total electromagnetic losses from 417 W to 349 W and improving steady-state efficiency from 93.7% to 95.1%. To overcome the inherent starting limitations of pure synchronous reluctance machines, an aluminum squirrel-cage is integrated to enable robust direct-on-line (DOL) synchronization, while NdFeB permanent magnets are embedded within the rotor flux barriers to mitigate asynchronous spatial harmonics and elevate torque density. Finite element analysis (FEA) confirms this magnetic assistance raises the average synchronous torque to 65.8 Nm while suppressing absolute torque ripple to 1.37 Nm. Finally, an evolutionary genetic algorithm is deployed across 440 iterative configurations to resolve geometric multi-physics conflicts. The finalized optimized design achieves a 13.2 kW output power at 1800 rpm, maximizing average torque to 70.12 Nm and strictly dampening absolute torque ripple to an industry-acceptable 1.04 Nm. Operating with an aggregated total loss of 1382 W, the optimized PMaNWLS-SynRM yields a 90.5% operational efficiency, definitively validating its suitability as an ultra-premium IE4/IE5 alternative to conventional induction motors.

Keywords: permanent magnet assisted line start synchronous reluctance motors (PMaLS-SynRM); nonoverlapping winding (NW); SynRM; LS-SynRM

Check for updates

Academic Editor: Wei Hua

Received: 7 March 2026
Revised: 13 April 2026
Accepted: 16 April 2026
Published: 18 April 2026

Copyright: © 2026 by the authors. Licensee MDPI, Basel, Switzerland. This article is an open access article distributed under the terms and conditions of the Creative Commons Attribution (CC BY) license.

1. Introduction

Continuous research to achieve ultra-premium efficiency in electrical machines has transformed the focus from conventional Induction machines (IMs) to magnet-free synchronous and hybrid topologies.

IMs dominate the industrial sector due to their simplicity and robustness, but their slip-based operation and rotor cage bar losses restrict higher efficiency attainability even

with modern materials and advanced manufacturing facilities [1,2]. Reducing the rotor resistance to minimize I^2R losses often degrades overall electromagnetic performance including torque density and direct-on-line (DOL) starting capability [3]. While advanced integrated loss optimization and sophisticated control tuning can significantly improve IM efficiency and dynamic response [1], the inherent presence of rotor Joule losses remains a primary physical hurdle for ultra-premium efficiency classes. Consequently, eliminating the rotor losses and the push toward IE4 and IE5 efficiency classes has prompted exploration of alternative machine topologies. A research demonstrated that an existing IMs when converted to an interior permanent-magnet (IPM) configuration raised efficiency to IE4 class without trading off reliability [4]. Another study similarly results that beyond the IE3 class, meaningful efficiency improvements require new electromagnetic principles such as synchronous reluctance (SynR) or permanent-magnet-assisted mode of operation [5]. These findings highlight that further improvement cannot rely solely on IM refinements, but the adoption of newer technologies is vital.

Synchronous reluctance motors (SynRMs) on the other hand replaces rotors conductor bars with a laminated salient rotor core comprising flux barriers. SynRMs generate torque through the saliency ratio, i.e., the difference between direct- and quadrature-axis (d-q axis) magnetic reluctance [5]. The absence of rotor currents in the core eliminates slip and associated copper loss, resulting in comparative efficiencies with premium IMs but with significantly reduced rotor heating [6]. The salient rotor produces less torque per ampere accompanied by a lower power factor (PF) [7]. Research over the past decade has concentrated on maximizing rotor saliency and torque density while controlling torque ripple and maintaining mechanical robustness. In [8] researcher outlines the strategies to enhance the SynRMs performance and classifies them into four domains, including rotor topology optimization, advanced magnetic materials, alternative winding schemes, and ripple-minimizing control. SynRMs are distinguished by their high efficiency and power density, which are obtained without resorting to rare-earth permanent magnets (PMs) and therefore are more economically effective and environmentally friendlier than Permanent Magnet Synchronous Machines (PMSMs), which rely on expensive and rare-earth materials [9].

SynRMs have reduced rotor losses compared to IMs due to the absence of rotor windings or bars, leading to improved efficiency, especially at constant speed operations [10]. SynRMs have a lower PF compared to IMs and PMSMs and may require larger converters and, therefore, higher overall system costs. SynRMs also do not have self-starting capability and need additional components or design modifications for starting, unlike IMs, which can be connected directly to the line. In torque performance, SynRMs can obtain similar or even superior torque densities compared to IMs but are afflicted with increased torque ripples due to their salient rotor configuration [11]. PMSMs have higher efficiency and power density, but an increased cost. The low startup performance of SynRMS is due to the absence of rotor winding or squirrel cage bars that could generate asynchronous torque during the startup. SynRMs rely purely on reluctance torque, which is not useful during startup as it requires the rotor to be synchronized with the stator's rotating magnetic field, requiring additional control strategies for better startup performance [12].

To mitigate torque pulsations in synchronous reluctance machines (SynRMs), a targeted optimization framework was developed in [13], wherein the spatial arrangement and geometric profiling of the rotor cage bars were specifically refined. This structural modification successfully suppressed torque ripple while concurrently elevating the aggregate electromechanical performance. Furthermore, the fundamental relationship between stator excitation and rotor topology was analyzed in [14], demonstrating that precise modulation of the current angle directly dictates the optimal rotor configuration and yields

notable performance enhancements. In a parallel effort to maximize torque density and minimize mechanical vibration, a novel geometric sizing strategy for the rotor flux barriers. specifically targeting their angular displacement and radial width was proposed [15]. By implementing this analytical approach, the average electromagnetic torque was augmented by 25.32%, accompanied by a substantial 76.92% attenuation in the absolute torque ripple profile.

Parallel research has examined stator configurations to reduce copper loss. Study presented in [16] implemented fractional-slot concentrated windings on a SynRM, by shortening end-turns and improving the slots fill factor resulting in slightly increased harmonic content. The prototype achieved predicted torque and efficiency, yet revealed the trade-off between compact winding layout and harmonic torque.The comparative study of different winding configurations for six-phase IMs is presented in [17]. The study involves dual three-phase, symmetrical and asymmetrical winding configurations using a reconfigurable 12-phase stator. The research analyzes the impact of different winding configurations on different machine parameters, including phase current quality and characteristic curves, resulting in a symmetrical six-phase stator with a single neutral offering a superior torque/current ratio under fault conditions.

The advanced nonoverlapping winding (NW) topology introduced in [18] represents an advancement in conventional motor design by achieving a 5.3% higher efficiency and 34% shorter axial length. NW reduces magnetomotive force (MMF) harmonics and end-winding losses while maintaining high winding factors [19]. The results demonstrated enhanced efficiency and reduced losses. Results from previous studies indicate that NW can accompany reluctance rotors for compact, high-efficiency machines, provided mitigation of harmonic content and improved electromagnetic performance. Modern SynRMs already attained IE4 class efficiency in variable-speed applications, but their inability of line start restricts direct replacement of IMs.

The limitation of direct on-line start without an inverter mechanism is overcome by Line-start synchronous reluctance motors (LS-SynRMs) by embedding a squirrel-cage in the salient rotor, allowing an identical induction start-up followed by synchronous operation. To achieve the LS mechanism, the rotor must satisfy induction torque phenomena during startup and reluctance torque conditions at steady state, making its design inherently multi-objective. In [20], a study considering rotor bridges and slot opening to increase the efficiency and PF of LS-SynRM is presented, which shows that by varying the rotor slot opening, d and q axis inductance's are changed. When the rotor slot is opened, the q-axis inductance decreases while the d-axis inductance increases and saturates. Hence, the PF can be improved, and the saliency ratio can be increased [13]. In [12], the author proposed a new design for LS-SynRM, in which the rotor conductor bar design, size, shape, and arrangement are designed based on the magnetic circuit difference between IM and SynRM. The results show improvement in starting torque fluctuations, providing a slight increase in PF and a structure that can be used to improve their line-start performance. The main drawback remains a relatively low PF (0.75–0.82) and limited synchronizing torque under high inertia loads, motivating the introduction of permanent-magnet assistance.

Permanent-magnet-assisted synchronous reluctance motors (PMa-SynRMs) embed small magnets, typically ferrite or NdFeB, into the rotor flux barriers to add up the reluctance torque with magnet torque. By utilizing only a fraction of PM, the air-gap flux, torque per ampere, and PF of the SynRM can be increased. A study optimized PM geometry in a PMa-SynRM resulting in maximized back-EMF and reduced torque ripples, achieving roughly 40% torque ripple reduction and higher torque density [21]. Another research examined a semi-overlapping winding (SW) arrangement added up with interior magnets reported a 1% efficiency increase and 20% lower torque ripple relative to

distributed-winding counterparts [22]. Furthermore, studies employing ferrite magnets achieved IE4 efficiencies and high PFs with negligible rare-earth material utilization, confirming PMa-SynRMs as cost-effective IE4/IE5 solutions. These machines exhibit up to 30% lower total losses and relatively higher torque density than pure SynRMs [23–26].

Building on these investigations, Integration of the cage bar structure of LS-SynRMs with the PM assisted rotor leads to the PMa-LS-SynRM. This type of machine provides a combination of asynchronous self-start, reluctance torque, and PM torque, aiming to deliver both direct-on-line start compatibility and IE4/IE 5-class efficiency. All reported PMa-LS-SynRMs utilize the conventional DW topologies. Even many of the studies contributing to rotor innovations or magnetic optimization opt the standard stator designs to ensure sinusoidal magneto-motive force (MMF) and predictable LS behavior. None of the surveyed papers to date explore or highlight NW in a direct-on-line PMa-SynRM context. This absence constitutes a clear research gap. NW could shorten end-turns, increase slot fill-factor, and reduce copper losses, directly contributing to IE4/IE5-level efficiency standards and ease in manufacturing. Unfilled stator slot construction design would also improve thermal management by opening multiple airflow paths. When combined with PM which already lowers current demand, these benefits could result in a noticeable overall loss reduction and compact motor architecture.

To explicitly demarcate the intellectual boundary between our foundational studies [27,28] and the present manuscript, it is necessary to clarify the current topological novelty. Our prior works were strictly unmagnetized, parametric investigations: the study in [28] evaluated rotor cage bar placement within a fixed non-overlapping winding (NW) topology, while [27] investigated cage bar geometry and winding connections. Neither of those previous studies incorporated permanent magnets, transient line-start analysis, or multi-objective optimization. The present manuscript introduces a genuinely new machine topology, the PMaNWLS-SynRM, by integrating permanent magnet assistance into the NW frame for the first time, fundamentally altering the air-gap flux density profile and torque composition. Rather than a simple amalgamation of existing technologies, the genuine novelty of this study is framed across three specific domains: (1) utilizing targeted PM assistance to actively counteract the severe spatial MMF harmonics introduced by non-overlapping windings, which traditionally degrade asynchronous line-starting capabilities; (2) establishing a direct DW versus NW comparative framework to isolate the impact of each topological shift under strict current-driven and isothermal boundary conditions; and (3) deploying an evolutionary Genetic Algorithm to navigate the severe multi-physics geometric conflicts between the concentrated stator, the induction cage, and the interior permanent magnets.

The remainder of this paper is organized as follows. Section 2 discusses the research methodology adopted in the current study. Sections 3 and 4 provides detailed analysis of the proposed machines by comparing different winding configurations along with comparative analysis of SynRM and LS-SynRM topologies respectively. Section 5 provides insights on the motor model subjected to multi-objective optimization providing the best performing model for industrial applications and Section 6 concludes the study.

2. Research Methodology

This section includes a comprehensive design process for the proposed machine models. The overall design process, including flux barrier design, cage bar design, placements, and winding topologies, is explained in detail. The dynamic properties of the proposed designs under both transient and steady-state analysis are calculated using the JMAG-Designer Version 23 software tool. The design concepts and initial setup of the indicated topologies are also presented. The dynamic performance of the proposed topologies is analyzed under several factors. The description of used materials, condition setup, cir-

cuit design, and NW is also incorporated. The general flow of the research process is demonstrated in Figure 1.

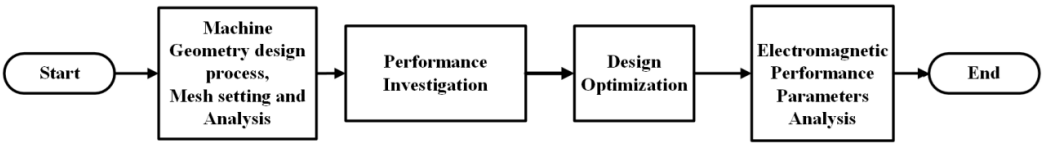

Figure 1. Flowchart of Methodology.

2.1. Design Methodology of the Proposed Machine Models

The work provides three SynRM variants with variable stator slots and squirrel cage designs in addition to the base machine with distributed winding, demonstrated in Section 3. These machines are referred to as DW-SynRM, DWLS-SynRM, NW-SynRM, NWLS-SynRM and PMaLS-SynRM. The materials used for all machines include 50A230 for rotor, copper for stator and aluminium for rotor cage bars, specifically in SynRMs with LS mechanism. DW-SynRM and DWLS-SynRM have 4-pole 36 slots, operating at 1800 rpm and 60 Hz frequency. Whereas the NW variants operating at same frequency and number of poles as the other variants but differ in stator slots arrangement, proposing a 2×12 multi-layer design. Furthermore, the inner shaft and outer diameter of all models are kept the same. The design parameters of the proposed machine are discussed in Table 1.

Table 1. Specifications of LS-SynRM with DW and NW.

Dimensions	DW	NW	Unit
Frequency	60		Hz
Pole/Slot	4/36	$4/2 \times 12$	-
Rotor Speed	1800		rpm
Stack Length	155		mm
Airgap Length	0.45		mm
Shaft Diameter	40		mm
Rotor Outer Diameter	139.1		mm
Machine Outer Diameter	235		mm
Mesh Size	1		mm
Upper Layer Turns/Coil	45	17	-
Lower Layer Turns/Coil	45	17	-
Stator Inner Diameter	140		mm
Current	15.06		A_{rms}
Core Material	50A230		-
Cage Material	Aluminium		-

2.2. Mathematical Model for Parametric Analysis of SynRM

The initial model includes a salient rotor with flux barriers. The starting characteristics and the performance of SynRM such as such as efficiency and power factor, are determined by the barrier design. Hence, the rotor slot design plays an important role in achieving synchronous speed, and barrier design is an important factor in satisfying the efficiency requirements of IE4/IE5. The PF of the NWSynRM is determined by the phase difference between current and voltage and can be expressed as,

$$\cos(\phi) = \frac{\rho - 1}{\sqrt{\frac{\rho^2}{\cos^2 \beta} + \frac{1}{\sin^2 \beta}}}, \rho = \frac{L_d}{L_q} \quad (1)$$

Synchronous Speed

There are no eddy currents in the rotor slot at synchronous speed because the slip is zero. Since both SynRM and NWSynRM operate at synchronous speed, their characteristics remain the same at synchronous speed, which can be expressed as:

$$\left(R_{arm}i_d - \omega_{eaf}L_q i_q\right)^2 + \left(R_{arm}i_q + \omega_{eaf}L_d i_d\right)^2 = V_{in}^2 \tag{2}$$

$$T_{reluct} = \frac{3}{2}\frac{N_p}{2}\left(L_d - L_q\right)i_d i_q \tag{3}$$

where armature resistance is represented by R_{arm}, electrical angular frequency ω_{eaf}, dq-axis inductances are represented as L_d and L_q, i_q and i_d are the dq-axis current, V_{in} the input voltage, T_{reluct} is the reluctance torque, and N_P is the number of poles. As mentioned before, the phase angle of the current increases due to the increase in d-q axis inductances, but the current's magnitude decreases. The performance of NWSynRM, such as PF and efficiency, is determined by the magnitude and phase angle of the current, which can be expressed as:

$$\eta = \frac{T_{reluct}\omega}{T_{reluct}\omega + P_{cp}(I_a) + P_{iron}(I_a,\ \beta)} \tag{4}$$

$$P_f = \frac{L_d/L_q - 1}{\sqrt{\left(L_d/L_q\right)^2/\sin^2\beta + 1/\cos^2\beta}} \tag{5}$$

where η is the efficiency, P_{cp} represents the copper loss, P_{iron} is the core loss, P_f is the power factor, and β is the phase angle.

To explicitly quantify the absolute mechanical pulsation that directly correlates to physical shear stress and acoustic resonance in industrial line-start drives, the absolute torque ripple (evaluated herein as the Ripple Rate) is calculated in Newton-meters (Nm) as the peak-to-peak excursion: Torque Ripples of the machine can be obtained by using Equation (6):

$$T_{rip_abs} = T_{max} - T_{min} \tag{6}$$

2.3. Efficiency Analysis

The electromagnetic efficiency (η) of the proposed topologies is evaluated by accounting for the discrete loss components extracted during the finite element analysis. Because the machine operates strictly as a motor, the mechanical output power (P_{out}) delivered at the rotor shaft is defined as the product of the average electromagnetic torque (T_{avg}) and the synchronous mechanical angular velocity (ω):

$$P_{out} = T_{avg}\omega \tag{7}$$

To sustain this mechanical output and overcome internal physics, the total active electrical input power (P_{in}) drawn at the stator terminals must satisfy the global power balance. Therefore, P_{in} is calculated as the sum of the mechanical output power and the total aggregated machine losses (P_{losses}):

$$P_{in} = P_{out} + P_{losses} \tag{8}$$

where P_{losses} encompasses the volumetric iron core losses (P_{iron}), mechanical losses, and the analytically corrected stator copper losses (P_{cu}) computed by the 2D FEA solver. Conse-

quently, the steady-state electromagnetic efficiency is derived as the ratio of the mechanical shaft power to the active electrical input power:

$$\eta = \frac{P_{out}}{P_{in}} \tag{9}$$

As,

$$P_{cu} = I^2 R = \frac{I^2 \rho L_{wire}}{A_{wire}} \tag{10}$$

where I, ρ, L_{wire}, and A_{wire} represent current (rms), resistivity ohm-m, length of the wire mm, and area of wire (mm^2), respectively. The area of the wire can be computed as

$$A = \frac{Sk_\omega}{N} \tag{11}$$

The S is the slot area, k_w represents the filling factor and N represents the number of turns. The slot area can be calculated from Equation (12), where J is the current density.

$$S = \frac{IN}{Jk_w} \tag{12}$$

Equation (10) becomes;

$$P_{cu} = I \rho J L_{wire} \tag{13}$$

Equation (13) can be used to calculate the copper loss on one wound. For the overall design, the copper loss can be computed by using Equation (14),

$$P_{Tc} = I \rho J L (NQ)(1000) \tag{14}$$

where Q represents the number of slot pairs.

2.4. FEA Boundary Conditions and Simulation Assumptions

To ensure absolute reproducibility and validate the comparative framework, a bifurcated excitation strategy was implemented within the 2D finite element analysis. Steady-state synchronous performance metrics; including average torque, torque ripple, and core losses, were extracted using a current-driven formulation fixed at 15.06 A rms, with the current angle β independently optimized to the maximum-torque-per-ampere (MTPA) trajectory for each respective topology. Conversely, the transient direct-on-line (DOL) synchronization analyses were evaluated using a voltage-driven model, governed by a stiff 460 V, 60 Hz grid supply under free-acceleration conditions. For this transient solver, the intrinsic rotor moment of inertia was rigorously computed as $J = 0.0301\ \text{kg} \cdot \text{m}^2$, ensuring the volumetric mass integration correctly accounted for the specific densities of the 50A230 laminated core, the cast aluminum cage, and the permanent magnets. No external load torque or coupled inertia was applied, thereby strictly isolating the inherent asynchronous pull-in capabilities of the machine.

Furthermore, thermal and spatial boundary constraints were codified to isolate the baseline electromagnetic phenomena. An isothermal boundary condition of 20 °C was uniformly applied across all models to define both conductor resistivity and permanent magnet remanence. While this omits the degradation inherent to high-temperature continuous operation, its uniform application strictly preserves the comparative integrity among the evaluated topologies. To compensate for the inherent spatial limitations of the 2D domain, end-winding copper resistance was analytically integrated into the phase resistance matrix by geometrically approximating the end-coil half-turn lengths for both

the distributed ($L_{ew} = \pi\tau_p/2$) and non-overlapping ($1.2\tau_c$) configurations. Although end-winding leakage inductance and axial flux fringing were excluded, standard simplifications in 2D cross-sectional solvers, these uniform omissions do not compromise the relative performance hierarchy established in this comparative investigation.

3. Performance Analysis of Synchronous Reluctance Motor

SynRM and Switched Reluctance Machine (SRM) are the most common types of Reluctance Machines. To apply the principle of reluctance torque, a rotating magnetic field and an anisotropic rotor are required. To achieve the anisotropy in rotor shape, the flux present in the d-axis should experience a low reluctance, while the q-axis is constrained by flux barriers or air barriers. The difference between d- and q-axis inductances, i.e., L_d & L_q also known as saliency ratio, is responsible for the torque production. In order to achieve maximum torque L_d should be maximized and L_q minimized. The equation for saliency ratio ζ and internal power factor (IPF) can be seen in Equations (15) and (16) respectively:

$$\zeta = \frac{L_d}{L_q} \tag{15}$$

$$IPF_{max} = \frac{\zeta - 1}{\zeta + 1} \tag{16}$$

While using a three-phase stator, the equation for torque expression needs to be changed and adapted according to the number of pole pairs, as presented previously in Equation (17). The equivalent circuit of SynRM in d-q axis reference is presented in Figure 2. Where the stator resistance R_{st} and leakage inductance L_l are liberated from the d and q reference. However, the magnetizing inductances L_{md} & L_{mq} differ from each other, resulting in different flux linkages, i.e., d & q flux linkages. Equations (17) and (18) serves as the governing equations depicting the electric behavior of SynRM, neglecting saturation.

$$\bar{v}_s = R_s\bar{i}_s + \frac{d\bar{\psi}_s}{dt} + j\omega_s\bar{\psi}_s \tag{17}$$

$$\bar{\psi}_s = L_{\sigma s}\bar{i}_s + \begin{bmatrix} L_{md} & 0 \\ 0 & L_{mq} \end{bmatrix}\bar{i}_s \tag{18}$$

A general term for a three-phase machine's torque can be expressed as Equation (19). After adding the stator flux and current, the resultant equation is Equation (20). If current excitation is applied to the machine, then the relation can be expressed as Equation (21). Equation (22) represents the torque equation for voltage-excited SynRM.

$$T_e = \frac{3n_p}{2}\,\mathrm{Im}\left(\bar{\psi}_s^*\bar{i}_s\right) \tag{19}$$

$$T_e = \frac{3n_p}{2}\left(\psi_{sd}i_{sq} - \psi_{sq}i_{sd}\right) = \frac{3n_p}{2}\left(L_{sd} - L_{sq}\right)i_{sd}i_{sq} \tag{20}$$

$$T_e = \frac{3n_p}{2}\left(L_{sd} - L_{sq}\right)I\sin(\delta_i)I\cos(\delta_i) = \frac{3n_p}{4}\left(L_{sd} - L_{sq}\right)I^2\sin(2\delta_i) \tag{21}$$

$$T_e = \frac{3n_p}{2} \cdot \frac{V^2}{2} \cdot \frac{(L_{sd} - L_{sq})}{(R_s^2 + X_d X_q)^2} \cdot \left\{ \left(X_d X_q - R_s^2 \right) \sin(2\delta_v) + R_s (X_q - X_d) - R_s (X_q + X_d) \cos(2\delta_v) \right\} \quad (22)$$

If stator resistance $R_s = 0$, the torque expression (Equation (22)) becomes the same as for a current-excited machine.

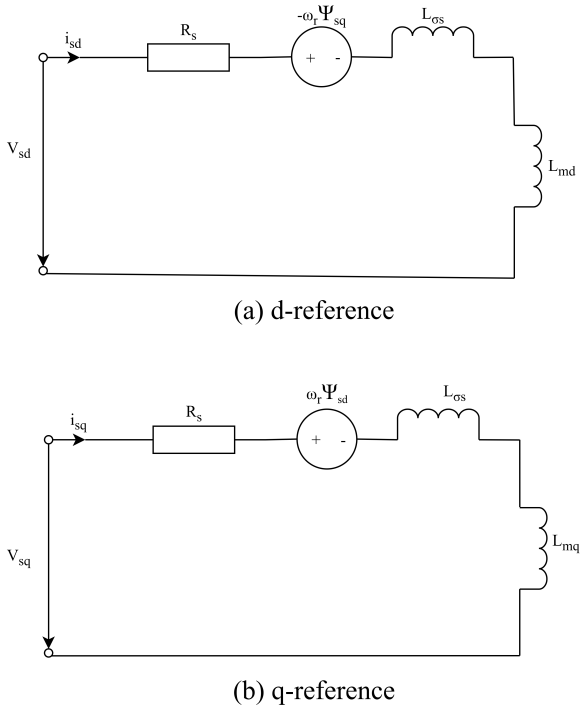

Figure 2. Equivalent circuit of SynRM in dq − components, neglecting iron loss.

3.1. Baseline Design Parameters and Operating Conditions

Both models (DW-SynRM and NW-SynRM) design characteristics are presented. The 2-D models can be observed in Figure 3a,b for DW-SynRM and NW-SynRM, respectively. The operating conditions of the machines are kept constant, running at 1800 rpm at 60 Hz frequency. Current density J_a is matched for both models, keeping I_{rms} the same and varying the number of turns, N, i.e., 17 and 45 for DW and NW-SynRM. Table 1 represents a comprehensive overview of the design parameters of both machines.

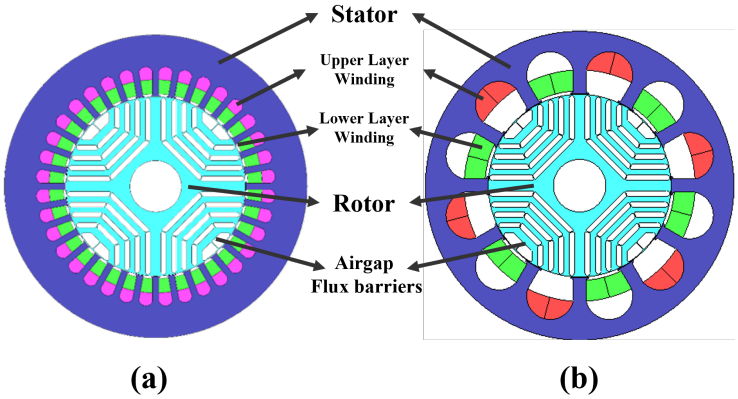

Figure 3. 2-D model of proposed SynRM with DW (**a**) and NW (**b**).

3.2. Winding Configuration

The winding configuration plays an important role in determining the overall electromagnetic performance of the machine. This section represents winding techniques adopted for SynRM. Winding layouts discussed include multi-layer DW and multi-layer NW. The NW topology uses both windings of stator slots, i.e., the upper and lower layers. Half of the slot area is kept unfilled to prevent overlapping of phase winding and better thermal management. The aforementioned winding configuration provides a reduction in end lengths and comprises shorter spans as compared to DWs. The unfilled stator slots, however, can cause an increase in the saturation levels but are beneficial in increasing the overloading capability of the machine. The winding diagram of DWSynRM and NW-SynRM are shown in Figures 4a and 4b respectively.

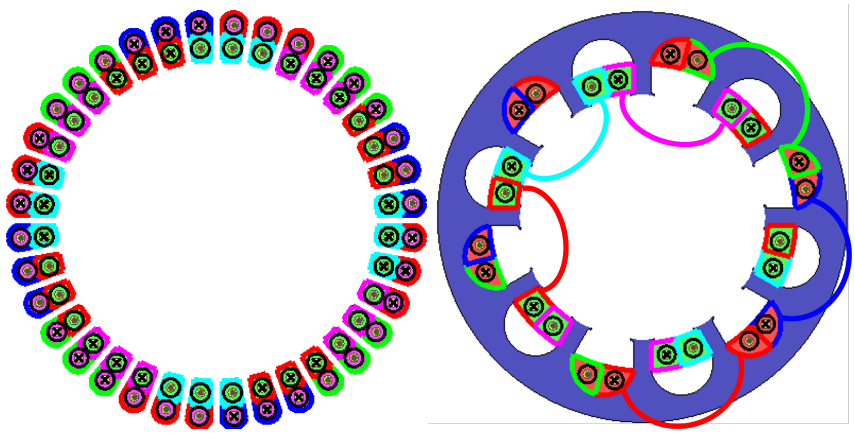

(**a**) (**b**)

Figure 4. (**a**) Winding diagram of 36 × 2 slot 4-pole DW-SynRM (**b**) Winding diagram of 2 × 12 slot 4-pole NW-SynRM.

3.3. Electromagnetic Performance

This section involves a comprehensive electromagnetic performance analysis of a SynRM with distributed and nonoverlapping winding. This analysis is performed under the same current loading for both models in terms of average torque, torque ripples, iron loss, copper loss, and overall efficiency of the machine.

3.3.1. Instantaneous Torque

Instantaneous Torque for NW SynRM and DW SynRM is presented in Figure 5. Results show that DW produces 33.2 Nm, whereas 36.6 Nm of torque was observed for NW. The torque comparison for both models is conducted under the same loading conditions for 15 A rms. The current density is matched for both models. DW SynRM comprises 17 turns/coil, whereas NW SynRM has 45 turns/coil.

3.3.2. Torque Ripples

The absolute torque ripple comparison for both winding models is presented in Figure 6b. It can be observed that DW exhibits a lower ripple rate of 1.45 Nm, whereas the content was higher in the case of NW, i.e., 1.61 Nm. The difference is due to the magnetomotive force content present in both cases. Due to the sinusoidal content present in the case of DW, the torque ripples were lower, whereas the NW exhibits a non-sinusoidal waveform for MMF.

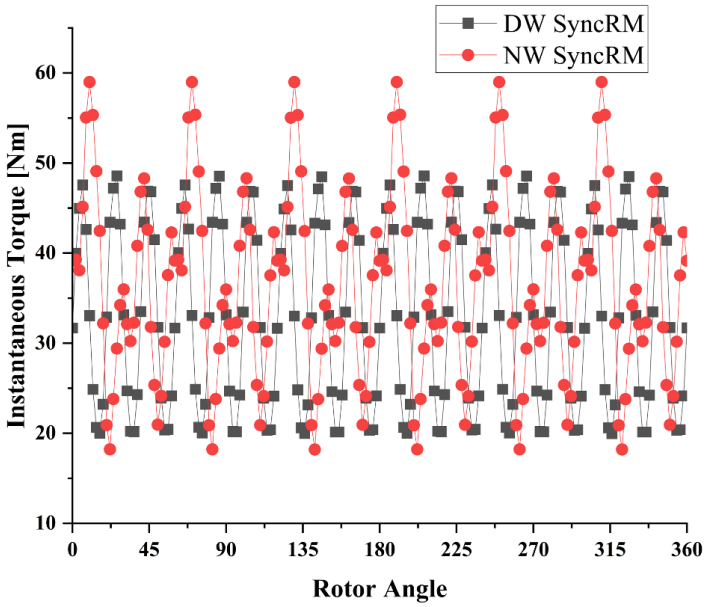

Figure 5. Instantaneous steady-state electromagnetic torque profiles of the evaluated machine variants.

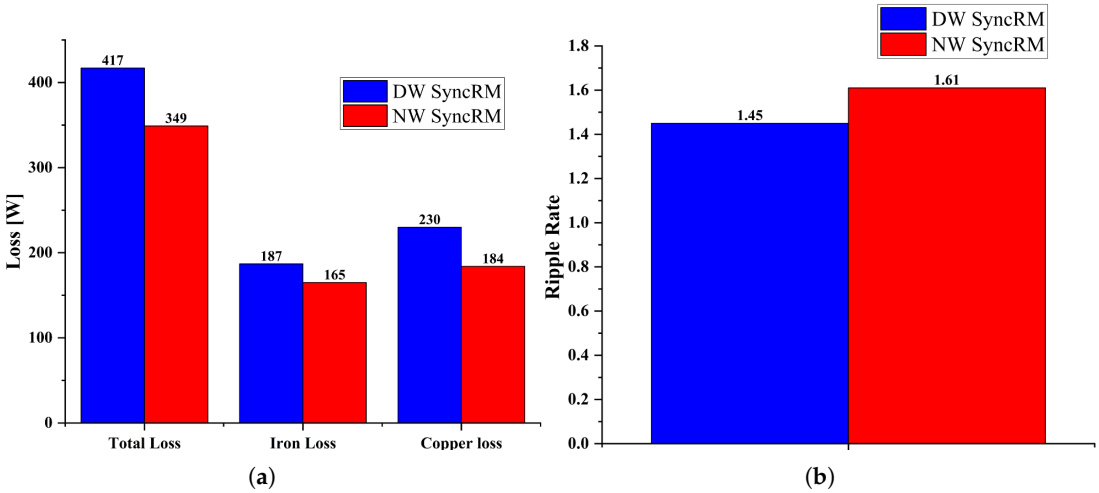

Figure 6. (**a**) Total Loss comparison of DW and NW SynRM (**b**) Torque Ripples comparison of DW and NW SynRM.

3.3.3. Iron Loss and Copper Loss

Figure 6a represents a total electromagnetic loss comparison between the DW and NW SynRM topologies. DW depicts higher losses, 230 W, due to end winding, whereas 184 W is observed for NW. On the other hand, lower iron/core losses were observed for NW, i.e., 165 W, compared with 187 W in the case of DW. The loss reduction in NW suggests improvement in the overall electrical efficiency of the motor, making it a substantial choice in terms of better thermal management and energy efficiency.

3.3.4. Output Power and Efficiency

The overall performance comparison for both machines is presented in Table 2. The results show that Nonoverlapping Winding produces a higher output power of 7 kW than the 6.2 kW produced in the case of distributed winding. Due to lower losses and better torque production, NW SynRM stands at an overall efficiency of 95.1%, 1.4% higher than the efficiency in the case of DW SynRM.

Table 2. Performance comparison for NW and DW.

Parameters	DW	NW	Unit
P_{out}	6.2	7	kW
Speed	1800		rpm
T_{rel}	33.2	36.6	Nm
I_{rms}	15.06		A
P_{core}	187	165	W
P_{copper}	230	184	W
Ripple Rate	1.45	1.61	Nm
Total Loss	417	349	W
Efficiency η	93.7	95.1	%

4. Performance Analysis of Line Start Synchronous Reluctance Motor

To overcome the non-starting ability of the SynRM, flux barriers/air-gap flux barriers can be equipped with cage bars. The cage bars, usually made of aluminum, are inserted in the air barriers, which introduce positive starting torque during startup of the machine. Cage bars also help the machine to run in synchronism. When synchronism is reached, then there is no voltage induced in the cage bars, and the losses are reduced as compared to the IM. Figure 7 illustrates the equivalent circuit of the LS-SynRM in dq quantities.

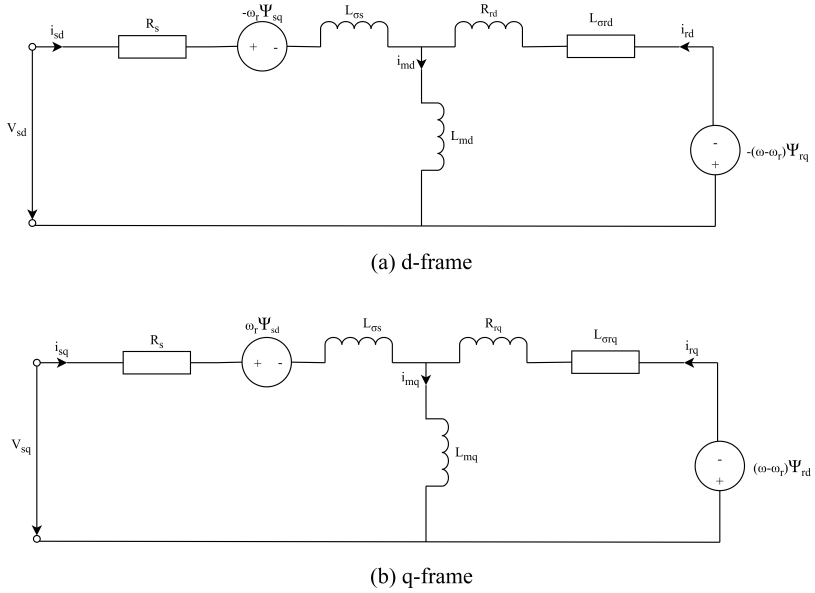

Figure 7. Equivalent circuit of LS-SynRM in dq − components.

As the cage bar influences the torque performance so the electrical torque during startup becomes a product of cage and reluctance torque, As shown in Equation (23).

$$T_e = \frac{3n_p}{2} \operatorname{Im}\left(\bar{\psi}_s^* \bar{i}_s\right) = T_{\text{cage}} + T_{\text{rel}} \tag{23}$$

The contribution of cage bar and reluctance torque can be calculated according to Equations (24)–(27). The torque produced by cage bars exhibits a constant value for different slip values. The cage is presumed to accelerate the speed of the machine to asynchronous speed close to synchronous speed. Whereas, it is observed that the contribution of reluctance torque is a trigonometric function oscillating with a value double that of the slip frequency.

$$T_e = T_{\text{cage}} + \hat{T}_{\text{rel}} \cdot \sin(2s\omega t - \alpha) \tag{24}$$

$$T_{\text{cage}} = \frac{3n_p}{4} \cdot (ce + df - ga - bh) \tag{25}$$

$$\hat{T}_{\text{rel}} = \frac{3n_p}{4} \sqrt{(ce + bh - df - ga)^2 + (ed + cf - gb - ah)^2} \tag{26}$$

$$\alpha = \arctan\left(\frac{gb + ah - ed - cf}{ce + bh - df - ga}\right) \tag{27}$$

When introducing a rotor resistance higher in the d-reference than the q-axis reference or vice versa, the torque gets distorted. This phenomenon, known as George's phenomenon, is known for induction motors with unbalanced rotors. However, the reluctance torque requires unsymmetrical magnetizing inductances, which inhibits the design of a symmetrical rotor resistance. After a successful run-up and synchronization, the rotor cage bar contribution is annihilated. The same torque equation described in Equation (22) is followed at synchronous speed at steady state.

4.1. Asynchronous Speed

At asynchronous speed, the LS-SynRM experiences slip, causing an induced voltage to be generated in the rotor slot conductors. This induced voltage produces magnetic torque, which helps the LS-SynRM achieve synchronization. In the case of NWSynRM, the reluctance torque is generated due to the saliency. Saliency is the difference between the d-q axis inductance. The torque can be expressed as

$$T_{asyn} = T_{mag} + T_{reluct} sin(2s\omega t + \alpha) \tag{28}$$

where T_{asyn} is the torque at asynchronous speed, T_{mag} is the magnetic torque due to the induced current, T_{reluct} is the torque produced by the saliency, s represents the slip, ω is the angular frequency, and α is the phase angle of the pulsating torque.

During asynchronous operation, the total electromagnetic torque comprises of two components, i.e., the induction torque (slip dependent) responsible for providing a positive average accelerating torque, similar to an induction motor. and the second component is reluctance torque (pulsating torque) which pulsates at twice the slip frequency with an average value of zero. The maximum load torque against which the rotor can successfully synchronize is defined as the pull-in torque, whereas the maximum torque the motor can sustain while being at synchronous speed is known as the pull-out torque.

4.2. Motor Model Development

This section involves the model development and design of LS-SynRM. Both models' (NWLS-SynRM and NWPMaLS-SynRM) design characteristics are presented. The 2-D models can be observed in Figure 8a,b for NWLS-SynRM and NWPMaNWLS-SynRM, respectively. The operating conditions of the machines are kept constant, running at 1800 rpm at 60 Hz frequency. Table 1 represents a comprehensive overview of the design parameters of both machines. Winding configurations are the same for both models, as discussed earlier.

For the PMaNWLS-SynRM variant, the magnetic assistance is provided by Arnold N42SH Neodymium-Iron-Boron (Nd-Fe-B) permanent magnets. The key magnetic properties evaluated under the 20 °C isothermal boundary condition include a remanent flux density (B_r) of 1.3 T and an intrinsic coercivity (H_{cj}) of −1600 kA/m. The total active magnet volume embedded within the rotor flux barriers is 133,808.4 mm^3.

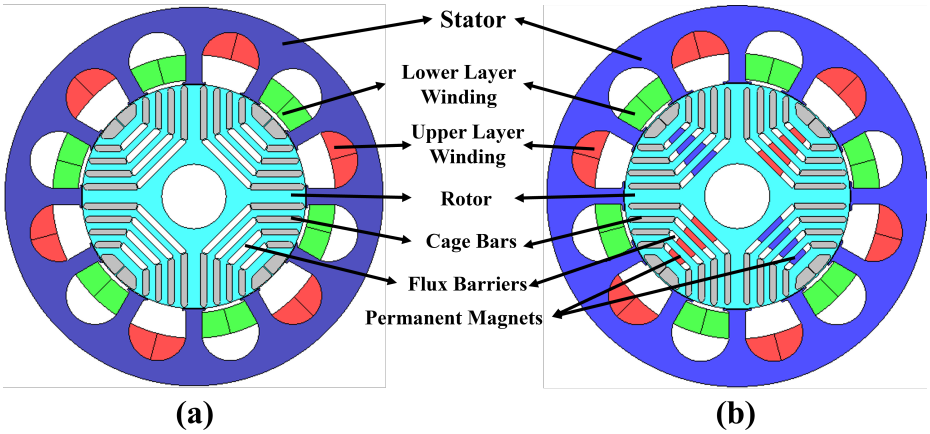

Figure 8. 2-D model of proposed NW-SynRM with LS (**a**) and PM-assisted (**b**).

4.3. Inductance Calculation

The direct and quadrature axis inductances, namely d- and q-axis inductances, can be calculated using the Equations (29) and (30). d-axis inductance:

$$L_d = \frac{3\psi_{max}}{2I_d}(H) \tag{29}$$

q-axis inductance:

$$L_q = \frac{3\psi_{min}}{2I_q}(H) \tag{30}$$

where ψ_{max} and ψ_{min} are the d- and q- axis flux linkages. I_d and I_q are the direct and quadrature axis currents, respectively. The flux linkages L_d, L_q, I_d, I_q and comparative analysis of saliency with respect to the current magnitude are presented in Figures 9, 10 and 11, respectively.

The graphs exhibit the fundamental behavior for all models of LS-SynRM with a positive saliency ratio, i.e., $\zeta = L_d/L_q > 1$ satisfying Equation (16). The magnetic saturation's effect, observed in the pronounced decrease L_q at higher currents, while the L_d remains more stable due to the flux barrier domination.

4.4. Transient Analysis of the Proposed Machine

While designing the synchronous reluctance machine, it is necessary to design the rotor flux barriers in such a way that the saliency ratio is maximum in to order to achieve better electromagnetic performance. Furthermore, the main advantage of the proposed machine is its ability to start directly on line without any need for an inverter mechanism. To achieve the line start ability, the rotor bars are designed in such a way that the machine can reach the synchronous speed fast and reliably. The initial analysis has been carried out using the FEM to examine the proposed NWLS-SynRMs startup behavior.

For a fair comparison, all the conditions as discussed in Table 1 are kept the same for all models.

The dynamic transient response of the electromagnetic torque for both models is illustrated in Figure 12. Anchoring this behavior to the analytical formulations presented in Equations (24)–(27), the initial transient phase is strictly dominated by the asynchronous cage torque (T_{cage}). During this immediate start-up period, the motor exhibits massive breakaway torque peaks exceeding 1000 Nm, a necessary electromechanical phenomenon to overcome the static rotor inertia under direct-on-line conditions. In the subsequent transient phase, as the motor accelerates and slip decreases, the induction torque contribution decays, and the slip-dependent pulsating reluctance torque ($\hat{T}_{rel}$) becomes the dominant

oscillatory component. Finally, as the slip approaches zero, the asynchronous pulsations are annihilated, and the motor successfully pulls into steady-state synchronism, depicting a lower-amplitude ripple centered around its respective average torque.

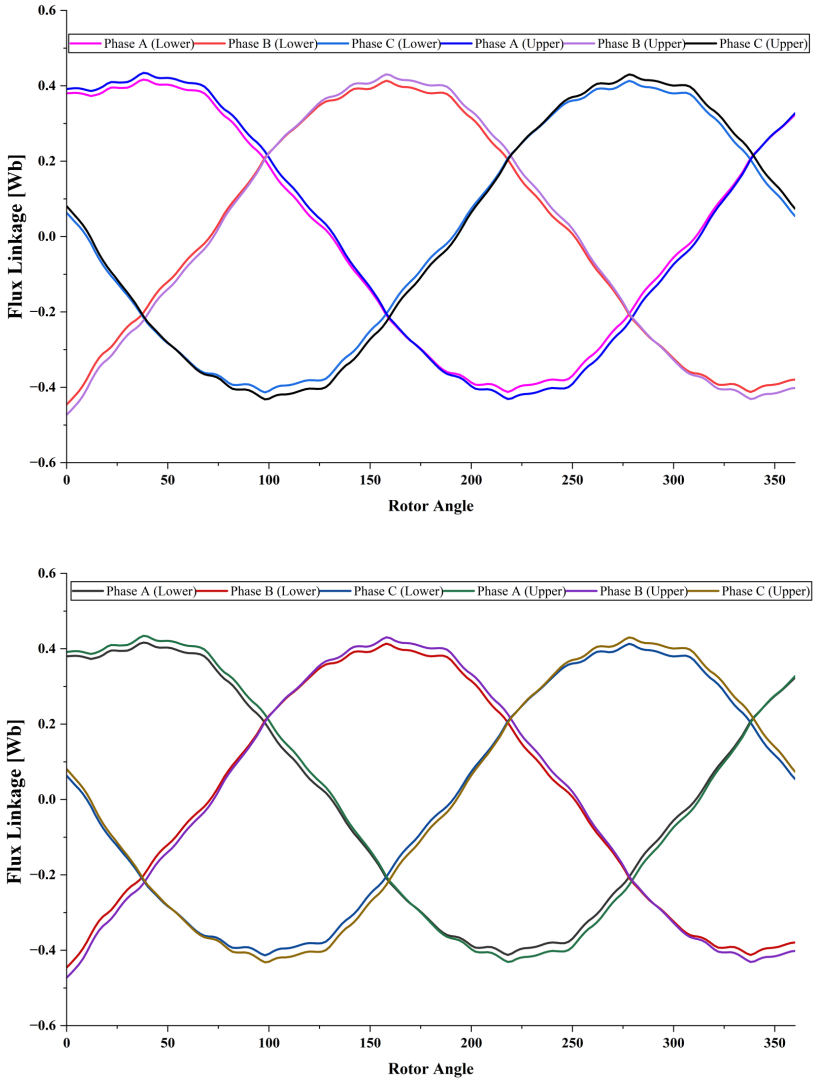

Figure 9. Flux Linkages of proposed models NWLS-SynRM (**upper**) and NWPMaLS-SynRM (**lower**).

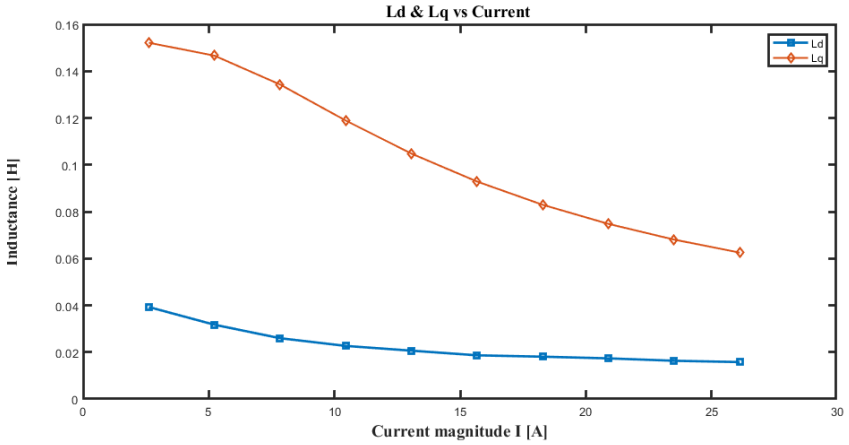

Figure 10. d- and q-axis inductances plot of the NWLS-SynRM at different current values.

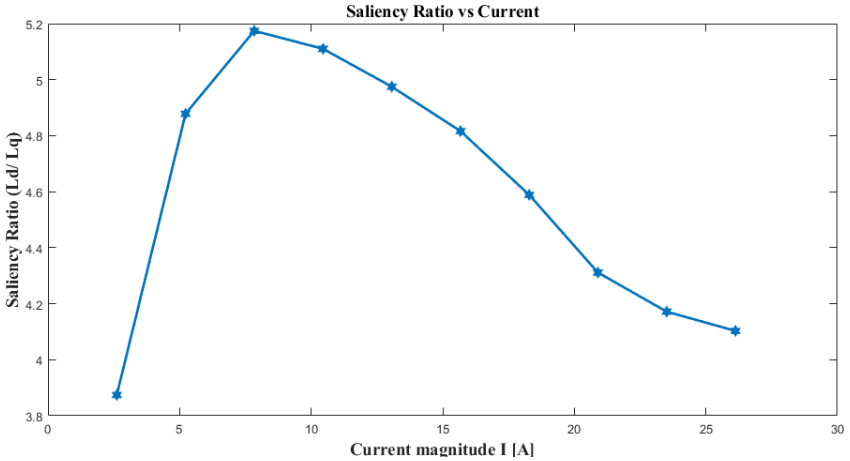

Figure 11. Saliency comparison of proposed NWLS-SynRM.

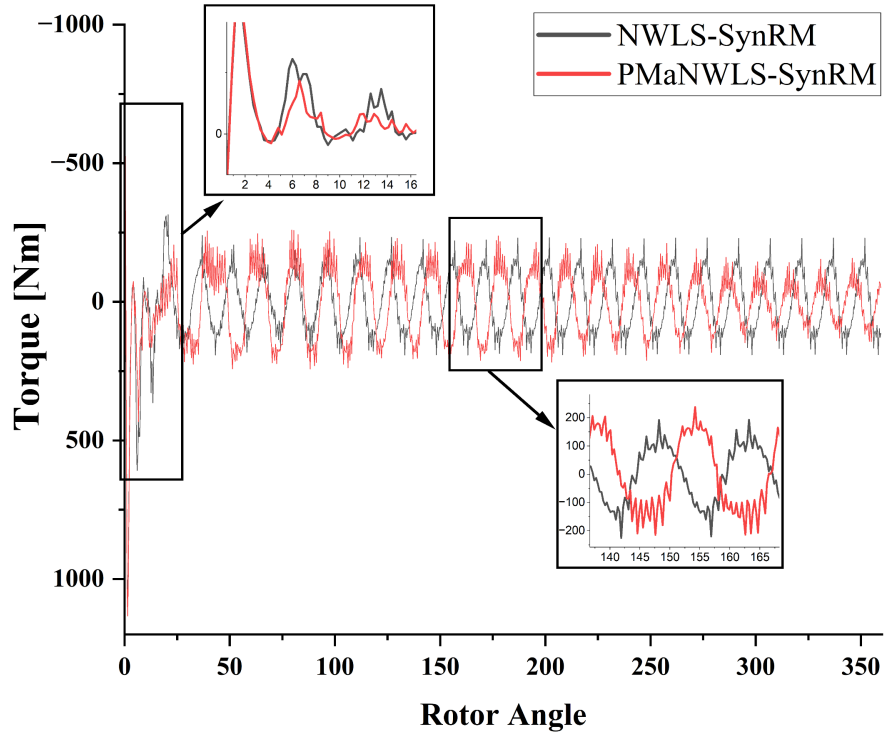

Figure 12. Transient torque waveforms of the proposed NWLS-SynRM models.

Furthermore, Figure 13 depicts the dynamic free-acceleration speed response during this line-start operation. While both models successfully pull into the 1800 rpm synchronous speed, the comparative advantage of the proposed magnetic hybridization is evident. The PMaNWLS-SynRM exhibits superior damping characteristics during the oscillatory pull-in phase, achieving stable synchronization significantly faster and with less severe overshoot relative to the unmagnetized NWLS-SynRM variant.

Figure 14, which indicates the coil flux linkages at the transient stage. The results indicate that the proposed models were able to produce nearly identical and robust torque profiles, providing a positive average torque. The high initial torque value indicates the motor's ability to start reliably from a steady state.

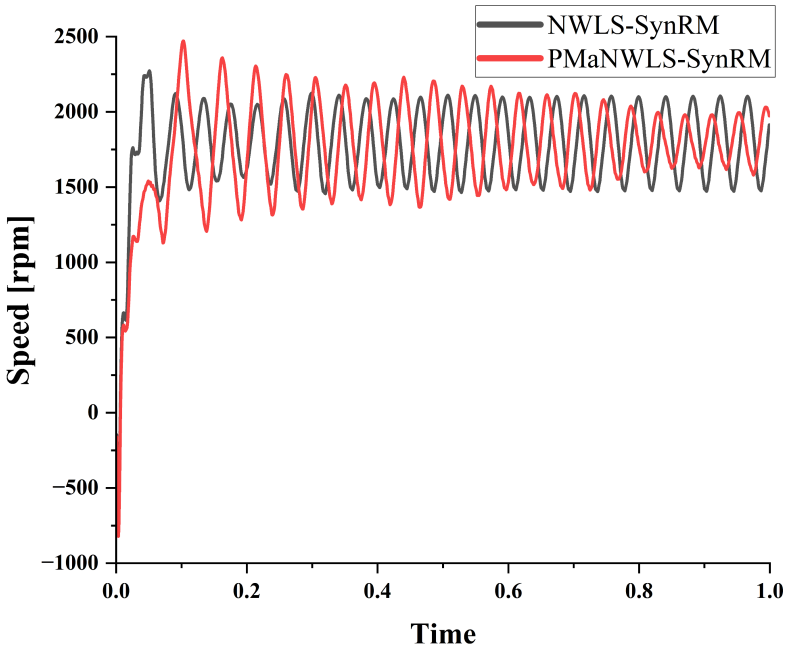

Figure 13. Starting speed vs time plot (free acceleration) of the proposed models of NWLS-SynRM.

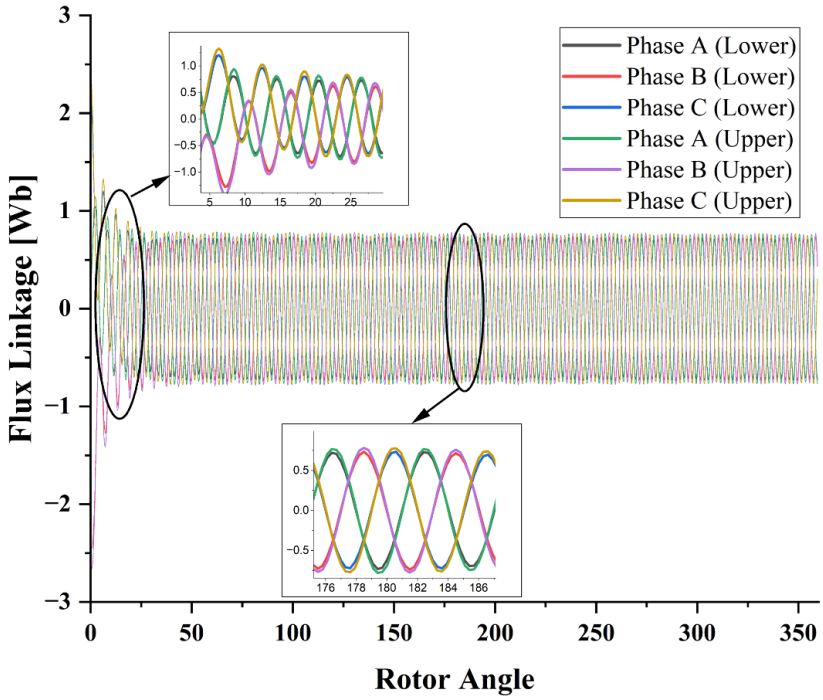

Figure 14. Coil Flux Linkage waveforms of the proposed NWLS-SynRM models.

4.5. Airgap Flux Density

Figure 15 shows the air-gap flux density comparison of the proposed models, evaluated precisely along the mid-air-gap contour to ensure physically accurate extraction. The unmagnetized NWLS-SynRM exhibits a peak air-gap flux density of ±1.15 T, safely within the saturation limits of the 50A230 electrical steel. Upon the integration of permanent magnets, the PMaNWLS-SynRM experiences a localized enhancement due to the additive magnetic loading, yielding a higher peak air-gap flux density of ±1.35 T. The superior characteristics of the PM-assisted version highlight that the machine achieves its electromagnetic torque with lower losses and an improved power factor. This reduction in the

losses and improvement in the power factor is due to the magnets providing the flux and reducing the required magnetizing current.

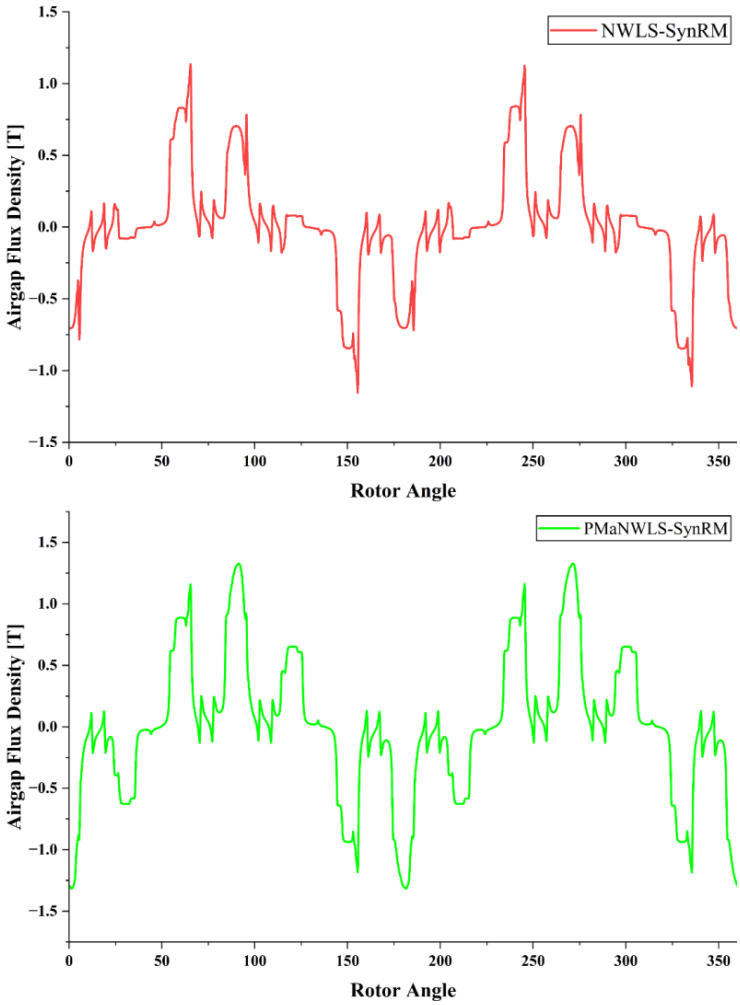

Figure 15. Airgap flux density comparison of the proposed models.

4.6. Instantaneous Torque

To ensure a rigorous and fair comparative analysis, the instantaneous torque and subsequent electromagnetic performance metrics for both the NWLS-SynRM and the PMaNWLS-SynRM were evaluated under identical rated stator current excitation (15.06 A rms). Evaluating the topologies at the same supply current ensures that the stator copper losses remain equal, thereby providing a direct assessment of the enhanced torque density, power factor, and efficiency strictly attributable to the permanent magnet assistance. As shown in the Figure 16, the PMaNWLS-SynRM exhibits a higher instantaneous and peak torque, representing a superior torque profile and a higher torque density than its counterpart. As discussed earlier when PMs are used in a NWLS-SynRM, the torque ripples were reduced, so are in this case. The PM-assisted variants exhibit lower torque ripples i.e., 1.37 Nm, compared to the 1.67 Nm for the other model shown in Figure 17a. Whereas, the NWLS-SynRM, on the other hand, despite its simpler structure, produces a slightly lower average torque and higher ripple content compared to the PMaNWLS-SynRM, as discussed in Table 3. Overall, the PM-assisted machine offers a comparatively superior performance with a blend of higher torque and lower ripple content, making it a better alternative than its counterpart.

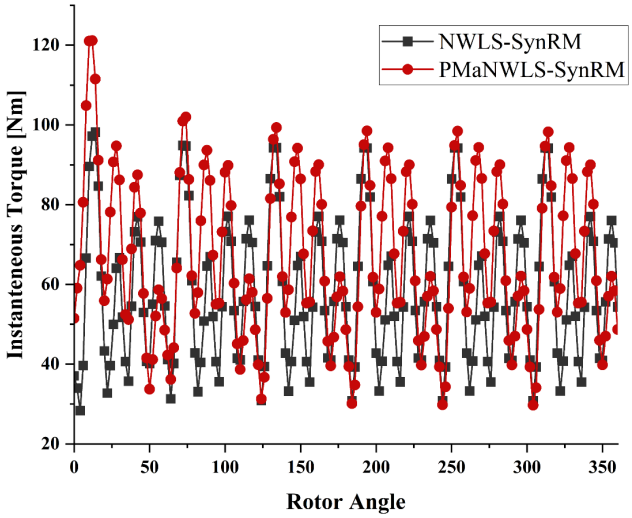

Figure 16. Instantaneous Torque waveforms of the proposed models.

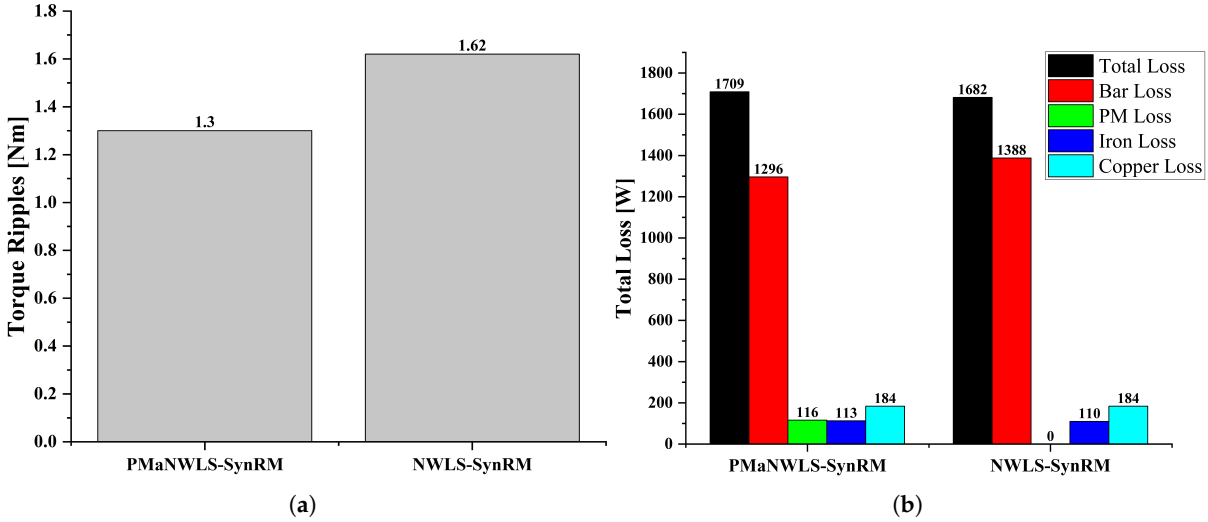

Figure 17. (**a**) Torque Ripple Comparison of the proposed models (**b**) Total Loss comparison of the proposed machines.

Table 3. Electromagnetic performance comparison of proposed models using FEA.

Parameters	NWLS-SynRM	PMaNWLS-SynRM	Unit
Torque	58.4	65.8	Nm
Torque Ripples	1.62	1.37	Nm
Rotor Bar Loss	1388	1296	W
Iron Loss	110	113	W
Copper Loss	184		W
PM Loss	0	116	W
Output Power	11	12.6	kW
Efficiency η	86.74	88.06	%

4.7. Total Losses

Total losses are very important in terms of calculating the overall electromagnetic performance of the machine. The losses taken into account for the above study include iron loss, rotor cage bar loss, and PM loss, shown in Figure 17b , indicating the influence of the PM assistance in the machine's loss distribution and overall electromagnetic efficiency of the machine. As shown in the figure, the most dominant loss in both machines is the rotor cage bar loss. However, a comparatively lower loss is observed in the PMaNWLS-SynRM due

to the rotor current loading and associated I^2R losses. PMs also introduce losses within the machine due to magnet hysteresis or eddy currents. Although PMs are naturally absent in the NWLS-SynRM version, PMs are also noticeably moderate in the PM-assisted version of the machine. Because the comparative framework enforces a strict current-driven boundary condition (fixed 15.06 A rms), the stator copper losses remain mathematically locked at 184 W for both topologies. However, as the integration of PM assistance inherently alters the localized magnetic flux density distribution, it results in a marginal, yet physically consistent, 3 W increase in volumetric iron loss (rising from 110 W in the unmagnetized NWLS-SynRM to 113 W in the PMaNWLS-SynRM). This minor penalty occurs because the bulk stator saturation is heavily dominated by the constant current excitation, meaning the fractional volume of the synchronously rotating permanent magnets produces only a minor perturbation in the alternating stator flux. The presented loss profile of the PM-assisted model suggests that PMs enhance the machine's electromagnetic performance. This increment in the performance is achieved through the reduction in the rotor current stress by improving the air-gap flux distribution eventually leading to better thermal management in the rotor by reducing the temperature. Table 3 shows a comprehensive overview of the electromagnetic performance of both models.

5. Multi-Objective Optimization (MOO) PMaNWLS-SynRM

A multi-objective optimization algorithm is employed to investigate the influence of different design parameters on the improvement of the initial electromagnetic performance of the proposed machine. The variables used in optimization are shown in Figure 18. Furthermore, the optimization results in the form of scattered plots are depicted in Figures 19a–d and 20 for average torque, torque ripples, iron loss, bar loss, and efficiency respectively. Comparison of proposed and optimized parameters are presented in Table 4.

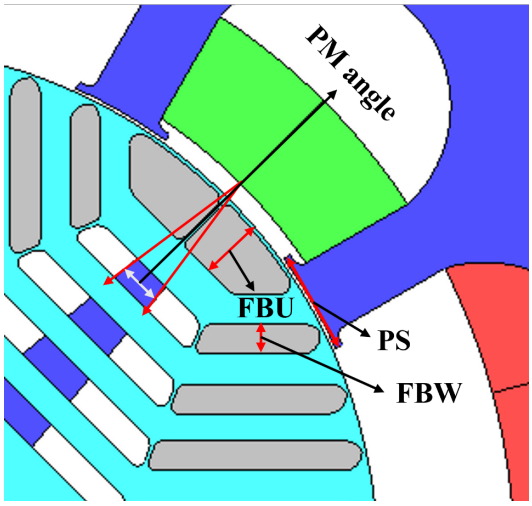

Figure 18. Optimization variables for the proposed machine.

To navigate the multi-variable design space and resolve the conflicting electromechanical objectives, a population-based Multi-Objective Genetic Algorithm (MOGA) was directly coupled with the finite element solver. The computational procedure was configured to evaluate a total of 440 iterative case studies, derived from an evolutionary structure of 20 generations with a population size of 22 individuals per generation ($22 \times 20 = 440$). During the evolutionary mutation process, strict geometric constraint handling was enforced. Specifically, extreme parametric combinations (e.g., conflicting barrier widths and pole shoe lengths) occasionally resulted in intersecting CAD boundaries, a non-physical geometric condition referred to as "region overlapping." Because these impossible geometries cannot

be physically manufactured or meshed by the FEA software, 33 such specimens were systematically discarded from the mating pool. This constraint-handling mechanism yielded 407 valid, successfully simulated machine configurations from which the Pareto-optimal front was derived. For the implementation of MOO, the objective function, set of variables to be optimized, and their respective ranges are defined as:

$$\begin{aligned} Objective\ Function = \ & Max\ (T_{avg}) \\ & Min\ (T_{rip}) \\ & Min\ (P_{iron}) \\ & Min\ (P_{bar}) \end{aligned}$$

$$Variables = Machine\ Parameters$$

$$Upper\ Flux\ Barrier\ Height = 6 \leq FBU \leq 8.25$$

$$Lower\ Flux\ Barrier\ Width = 3 \leq FBW \leq 5.5$$

$$Pole\ Shoe\ Length = 6 \leq PS \leq 12$$

$$Permanent\ Magnet\ Angle = 40 \leq PM_{anlge} \leq 60$$

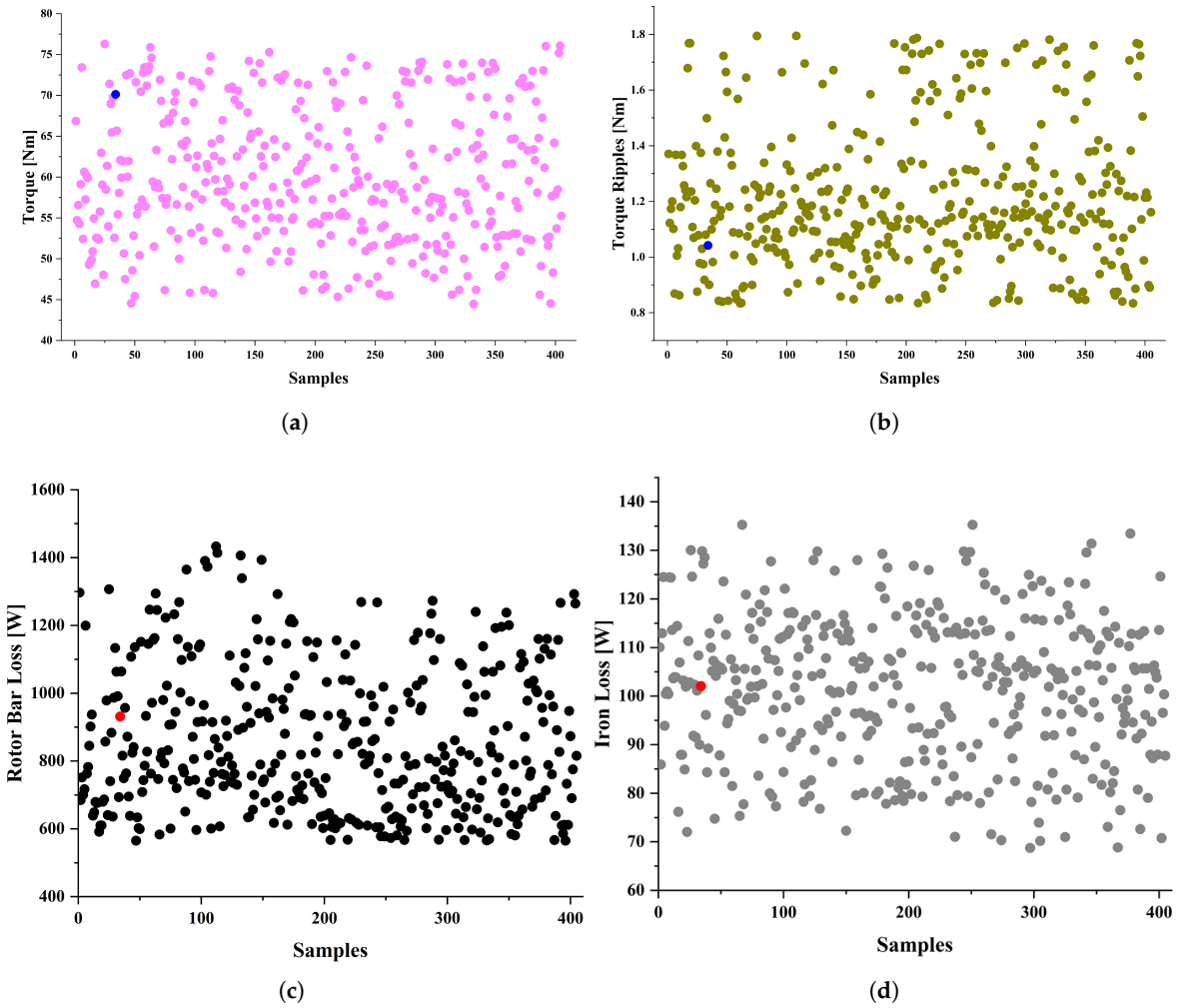

Figure 19. (**a**) Scatter plot for average torque (**b**) Scatter plot for torque ripple (**c**) Scatter plot for rotor bar loss (**d**) Scatter plot for iron loss.

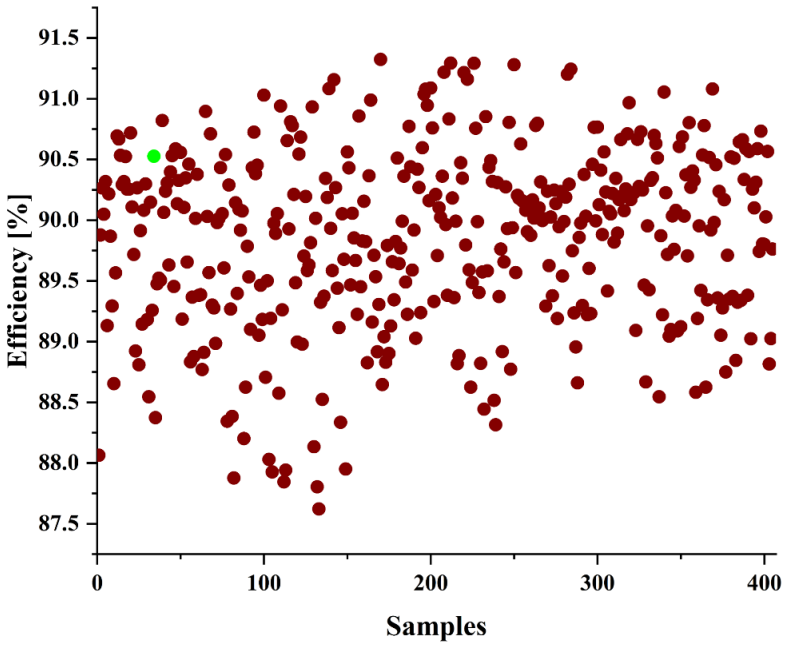

Figure 20. Scatter plot for efficiency.

Table 4. Design parameter comparison of before and after optimization.

Parameter	Initial	Optimized	Unit
FBU	8.25	6	mm
FBL	4	3.85	mm
PS	7	12	mm
PM_{angle}	50.19	56.7	degrees
Cage Bar Area	3928	3554	mm^2
PM utilization	509	533.5	mm^2

5.1. Electromagnetic Performance Comparison of the Unoptimized and Optimized Model

In this section, the electromagnetic performance is analyzed and compared using 2-D FEA between unoptimized (proposed) and optimized PMaNWLS-SynRM, including instantaneous torque, iron loss, rotor cage bar loss, torque ripple rate, and efficiency. The optimized design shows better performance, including higher average torque, lower torque ripples, lower iron and rotor cage bar losses, and higher efficiency.

5.1.1. Instantaneous Torque

Instantaneous torque is analyzed under loaded conditions for the investigated machines at 15 A rms. Instantaneous torque waveforms for PMaNWLS-SynRM and optimized PMaNWLS-SynRM are depicted in Figure 21. From the figure, it can be observed that the optimized model exhibits a higher average torque than the unoptimized model. The increase in torque with NWLS-SynRM is due to the increased PM volume and reduced cage bar utilization, which resulted in higher induced EMF. As a result, the current flow increased, which directly affected the torque performance of the machine.

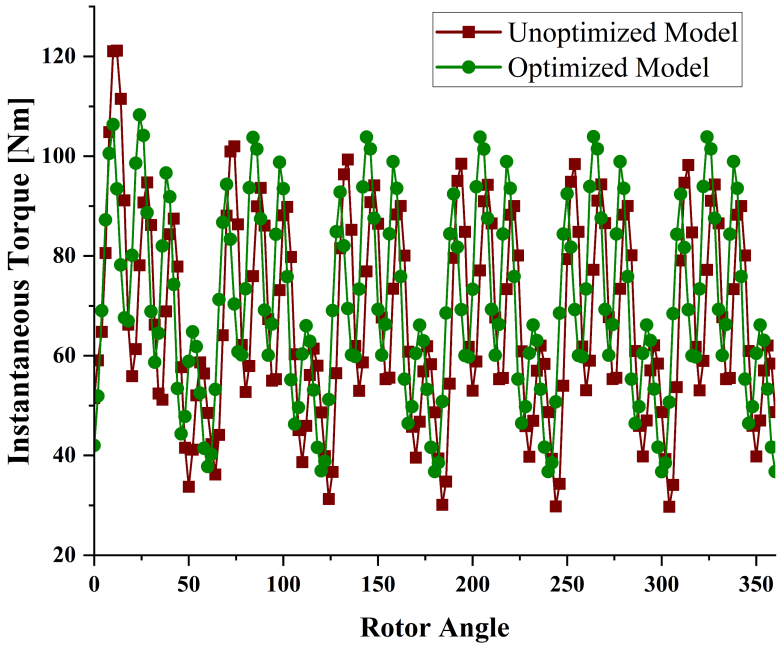

Figure 21. Instantaneous Torque comparison of unoptimized and optimized model.

5.1.2. Ripple Rate

Figure 22a shows the torque ripple rate comparison of borth models. The results clearly inidcate that the optimization effectively improves the torque profile by increasing the average torque and reducing torque ripples. Thre reduction in the torque ripples depicts stabilized torque production through smoothened air-gap flux distribution and harmonic ripple componenet mitigation.

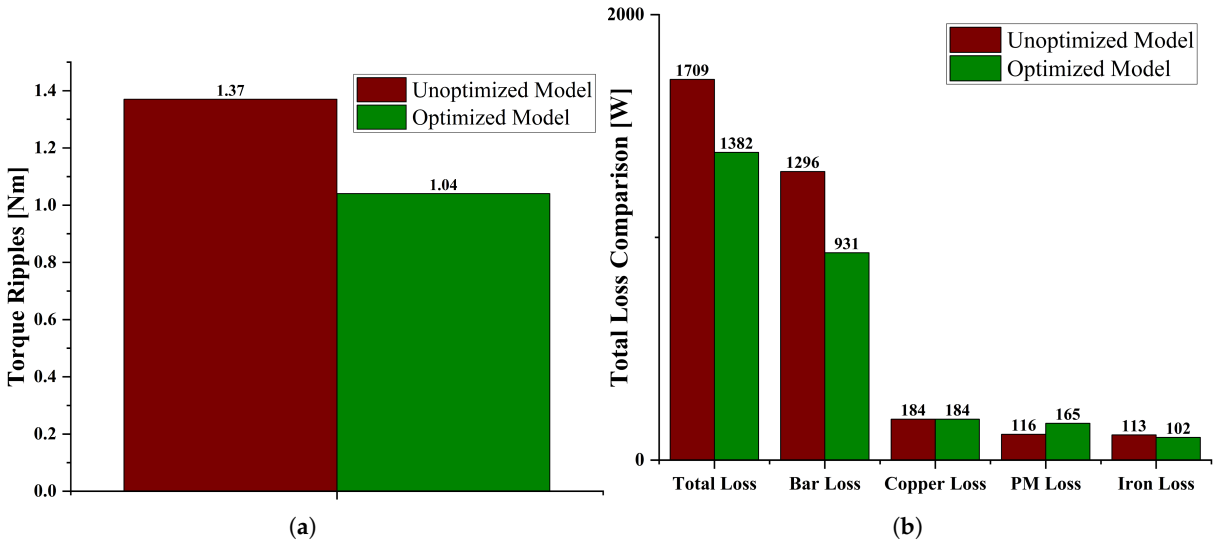

Figure 22. (**a**) Torque ripple comparison of unoptimized and optimized model (**b**) Total loss comparison of un-optimized and optimized model.

5.1.3. Total Loss and Efficiency

Figure 22b illustrates the total loss comparison of the unoptimized and optimized models.The graphs depict that optimized PMaNWLS-SynRM has lower losses than its counterpart. Unoptimized model indicates higher losses, resulting in decreased efficiency. The detailed comparison of investigated models of PMaNWLS-SynRM is presented in Table 5.

Table 5. Electromagnetic performance comparison of proposed and optimized model.

Parameters	Proposed Model	Optimized Model	Unit
P_{out}	12.6	13.2	kW
Speed	1800		rpm
T_{avg}	66.85	70.12	Nm
I_{rms}	15.06		A
P_{core}	113	102	W
P_{copper}	184		W
P_{bar}	1296	931	W
Ripple Rate	1.37	1.04	Nm
$Loss_{total}$	1709	1382	W
Efficiency η	88.06	90.5	%

6. Conclusions

This study has systematically investigated the topological progression and multi-objective optimization of a Permanent Magnet-assisted Non-overlapping Winding Line-Start Synchronous Reluctance Motor (PMaNWLS-SynRM). The comparative baseline analysis demonstrated that transitioning from a conventional distributed winding (DW) to a non-overlapping winding (NW) architecture fundamentally reduced end-turn copper lengths, decreasing total electromagnetic losses from 417 W to 349 W and elevating steady-state efficiency from 93.7% to 95.1%. To resolve the inherent starting limitations of pure synchronous reluctance machines, an aluminum squirrel-cage was integrated, enabling robust direct-on-line (DOL) synchronization with initial breakaway torques exceeding 1000 Nm. The subsequent integration of NdFeB permanent magnets within the rotor flux barriers significantly enhanced transient stability and torque density, raising the average synchronous torque to 65.8 Nm while reducing the absolute torque ripple to 1.37 Nm.

Finally, an evolutionary multi-objective genetic algorithm (MOGA) was deployed to optimally resolve the geometric multi-physics conflicts. The finalized PMaNWLS-SynRM design achieved a 13.2 kW mechanical output power at 1800 rpm, maximizing average torque to 70.12 Nm while strictly dampening the absolute torque ripple to 1.04 Nm. Operating with a minimized total loss of 1382 W, the optimized topology yielded a 90.5% efficiency, establishing it as a highly compact, robust, and energy-efficient alternative to conventional industrial induction motors. It should be noted that while the primary motivation of this architecture is the replacement of industrial IMs, the quantitative scope of this specific study is strictly bounded to the internal topological progression of the reluctance machine. Future investigations will therefore prioritize a direct empirical and computational benchmarking of the optimized PMaNWLS-SynRM against a fully optimized reference induction motor of identical frame size to definitively validate its industrial substitution potential.

Author Contributions: Conceptualization, S.T.H., F.K. and D.Y.U.; methodology, F.K.; software, D.Y.U. and W.K.; validation, D.Y.U. and W.K.; formal analysis, S.T.H., F.K., A.A., D.Y.U. and W.K.; investigation, S.T.H., A.A. and W.K.; resources, F.K. and D.Y.U.; data curation, S.T.H. and W.K.; writing—original draft preparation, S.T.H.; writing—review and editing, S.T.H., F.K., A.A., D.Y.U. and W.K.; visualization, S.T.H., A.A. and W.K.; supervision, F.K. and D.Y.U.; project administration, F.K., A.A. and D.Y.U.; funding acquisition, A.A. and D.Y.U. All authors have read and agreed to the published version of the manuscript.

Funding: This work was supported by Gyeongsang National University and the National Research Foundation of Korea (NRF) grant funded by the Korea government (MSIT) (RS-2025-16065383).

Data Availability Statement: All data supporting this study's findings are included in the article. No additional datasets were generated or used. Further details can be requested from the corresponding authors.

Acknowledgments: The authors gratefully acknowledge the researchers and staff of the Electric Machine Design Research (EMDR) Lab at COMSATS University Islamabad, Abbottabad Campus for providing a highly collaborative research environment. We sincerely appreciate the technical support, constructive discussions, and access to the computational resources that facilitated the design and analysis presented in this study.

Conflicts of Interest: The authors declare no conflicts of interest.

References

1. Konuhova, M. Induction Motor Dynamics Regimes: A Comprehensive Study of Mathematical Models and Validation. *Appl. Sci.* **2025**, *15*, 1527. [CrossRef]
2. Dhieb, Y.; Ayadi, W.; Malik, F.H.; Ambramoli, S.; Alkhatib, F.; Ghariani, M. Sliding Mode Controller Tuning Using Nature-Inspired Optimization for Induction Motor: EV Application. *World Electr. Veh. J.* **2025**, *16*, 559. [CrossRef]
3. Suli, S.; Öner, Y.; Şenol, İ. Design of SynRM and PMaSynRM using a common industrial stator platform: A new design methodology for transition from industrial applications to electric vehicles. *Eng. Sci. Technol. Int. J.* **2025**, *71*, 102204. [CrossRef]
4. Hofman, I.; Sergeant, P.; Van den Bossche, A. Conversion of standard induction machines to permanent magnet synchronous machines with higher efficiency. *Int. Rev. Electr. Eng.* **2012**, *7*, 5462–5473.
5. Liu, H.-C. Systematic Optimization Study of Line-Start Synchronous Reluctance Motor Rotor for IE4 Efficiency. *Machines* **2025**, *13*, 420. [CrossRef]
6. Chen, W.; Wang, Y.; Liu, X.; Shi, Y.; Zhao, Y.; Qu, R. Comparative Study of Hybrid PM Assisted Synchronous Reluctance Machines with Different Configurations. *IEEE Trans. Ind. Appl.* **2025**, *61*, 9269–9280. [CrossRef]
7. Heidari, H.; Rassõlkin, A.; Kallaste, A.; Vaimann, T.; Andriushchenko, E.; Belahcen, A.; Lukichev, D.V. A Review of Synchronous Reluctance Motor-Drive Advancements. *Sustainability* **2021**, *13*, 729. [CrossRef]
8. Li, Y.; Ma, B.; Zheng, J.; Zhu, J.; Lei, G. Electromagnetic and Mechanical Topology Optimization for SynRM Rotors Considering High Dimensional Constraints. *IEEE Trans. Ind. Electron.* **2023**, *70*, 12048–12059. [CrossRef]
9. Rebbah, M.Y.; Kaikaa, M.Y.; Boudjelida, L. Hybrid winding function method for inductance analysis of a line start synchronous reluctance machine. *Int. J. Electr. Comput. Eng. IJECE* **2022**, *12*, 4841–4851. [CrossRef]
10. Raziee, S.M.; Misir, O.; Ponick, B. Combined Star-Delta Winding Analysis. *IEEE Trans. Energy Convers.* **2018**, *33*, 383–394. [CrossRef]
11. Kersten, A.; Liu, Y.; Pehrman, D. Rotor Design of a Line-Start Synchronous Reluctance Machine with Respect to Induction Machine for Industrial Applications. In Proceedings of the 2018 XIII International Conference on Electrical Machines (ICEM) Alexandroupoli, Greece, 3–6 September 2018; pp. 393–399. [CrossRef]
12. Villani, M.; Fabri, G.; Credo, A.; Di Leonardo, L.; Parasiliti Collazzo, F. Line-Start Synchronous Reluctance Motor: A Reduced Manufacturing Cost Avenue to Achieve IE4 Efficiency Class. *IEEE Access* **2022**, *10*, 100094–100103. [CrossRef]
13. Ibrahim, M.N.F.; Sergeant, P.; Rashad, E. Simple Design Approach for Low Torque Ripple and High Output Torque Synchronous Reluctance Motors. *Energies* **2016**, *9*, 942. [CrossRef]
14. Xing, F.; Zhang, J.; Zhang, M.; Qin, C. Design and Multi-Objective Optimization of an Asymmetric-Rotor Permanent-Magnet-Assisted Synchronous Reluctance Motor for Improved Torque Performance. *Appl. Sci.* **2024**, *14*, 6734. [CrossRef]
15. Naeimi, R.; Nasiri-Zarandi, R.; Abbaszadeh, K. C- and circular-shaped barriers optimization in a synchronous reluctance rotor for torque ripples minimization. *Sci. Iran. Trans. D* **2023**, *30*, 1085–1096. [CrossRef]
16. Taghavi Araghi, S.M.; Kiyoumarsi, A.; Mirzaeian Dehkordi, B. Synchronous reluctance machines with new type of fractional-slot concentrated-windings based on the concept of stator slot shifting. *IET Electr. Power Appl.* **2023**, *17*, 92–108. [CrossRef]
17. Abdel-Khalik, A.S.; Abdel-Majeed, M.S.; Ahmed, S. Effect of Winding Configuration on Six-Phase Induction Machine Parameters and Performance. *IEEE Access* **2020**, *8*, 223009–223020. [CrossRef]
18. Gundogdu, T.; Zhu, Z.Q.; Mipo, J.C. Optimization and Improvement of Advanced Nonoverlapping Induction Machines for EVs/HEVs. *IEEE Access* **2022**, *10*, 13329–13353. [CrossRef]
19. Gundogdu, T.; Zhu, Z.-Q.; Mipo, J.-C. Design and Analysis of Advanced Nonoverlapping Winding Induction Machines for EV/HEV Applications. *Energies* **2021**, *14*, 6849. [CrossRef]
20. Kim, H.; Kang, J.; Kim, J.; Ahn, J.; Yun, I.; Lee, J.; Noh, Y. Design and Analysis of Line-Start Synchronous Reluctance Motor Considering the Maximum Inertia and Power Factor. *IEEE Trans. Ind. Appl.* **2023**, *59*, 5908–5918. [CrossRef]
21. Shah, S.H.; Mohammed, O.M.E.; Rahman, S.U.; Cai, H. Synchronous reluctance machine design considering slotting effect and rotor topology optimization. *Eng. Sci. Technol. Int. J.* **2025**, *69*, 102140. [CrossRef]
22. Dwivedi, S.; Tripathi, S.M.; Sinha, S.K. Review on Control Strategies of Permanent Magnet-Assisted Synchronous Reluctance Motor Drive. In Proceedings of the 2020 International Conference on Power Electronics & IoT Applications in Renewable Energy and its Control (PARC), Mathura, India, 28–29 February 2020; pp. 124–128. [CrossRef]

23. Nobahari, A.; Vahedi, A.; Zarandi, R.N. A modified permanent magnet-assisted synchronous reluctance motor design for torque characteristics improvement. *IEEE Trans. Energy Convers.* **2022**, *37*, 989–998. [CrossRef]
24. Mohammadi, A.; Mirimani, S.M. Design of a novel PM-assisted synchronous reluctance motor topology using V-shape permanent magnets for improvement of torque characteristic. *IEEE Trans. Energy Convers.* **2022**, *37*, 424–432. [CrossRef]
25. Gallicchio, G.; Di Nardo, M.; Palmieri, M.; Marfoli, A.; Degano, M.; Gerada, C.; Cupertino, F. High speed permanent magnet assisted synchronous reluctance machines—Part I: A general design approach. *IEEE Trans. Energy Convers.* **2022**, *37*, 2556–2566. [CrossRef]
26. Korman, O.; Di Nardo, M.; Degano, M.; Gerada, C. A novel flux barrier parametrization for synchronous reluctance machines. *IEEE Trans. Energy Convers.* **2022**, *37*, 675–684. [CrossRef]
27. Haider, S.T.; Khan, F.; Um, D.-Y.; Khan, W.; Rafique, K. Effect of Rotor Bar Placement on the Electromagnetic Performance of Nonoverlapping Winding Synchronous Reluctance Motors. In Proceedings of the 2025 28th International Conference on Electrical Machines and Systems (ICEMS), Busan, Republic of Korea, 16–19 November 2025; pp. 792–797. [CrossRef]
28. Haider, S.T.; Khan, F.; Um, D.Y.; Khan, W. Design and Analysis of Nonoverlapping Winding Line Start Synchronous Reluctance Motor. *IEEJ J. Ind. Appl.* **2026**, *15*, 293–302. [CrossRef]

Disclaimer/Publisher's Note: The statements, opinions and data contained in all publications are solely those of the individual author(s) and contributor(s) and not of MDPI and/or the editor(s). MDPI and/or the editor(s) disclaim responsibility for any injury to people or property resulting from any ideas, methods, instructions or products referred to in the content.